RESEARCH ARTICLE

Modeling of transverse stimulated Raman scattering in KDP/DKDP in large-aperture plates suitable for polarization control

Hu Huang[1], Tanya Z. Kosc[1,2], Terrance J. Kessler[1], and Stavros G. Demos[1]

[1] *Laboratory for Laser Energetics, University of Rochester, Rochester, NY, USA*

[2] *Currently at Khiram Prototype Works LLC, Rochester, NY, USA*

(Received 10 February 2023; revised 20 April 2023; accepted 17 May 2023)

Abstract

Transverse stimulated Raman scattering (TSRS) in potassium dihydrogen phosphate (KDP) and deuterated potassium dihydrogen phosphate (DKDP) plates for large-aperture, inertial confinement fusion (ICF)-class laser systems is a well-recognized limitation giving rise to parasitic energy conversion and laser-induced damage. The onset of TSRS is manifested in plates exposed to the ultraviolet section of the beam. TSRS amplification is a coherent process that grows exponentially and is distributed nonuniformly in the crystal and at the crystal surfaces. To understand the growth and spatial distribution of TSRS energy in various configurations, a modeling approach has been developed to simulate the operational conditions relevant to ICF-class laser systems. Specific aspects explored in this work include (i) the behavior of TSRS in large-aperture crystal plates suitable for third-harmonic generation and use as wave plates for polarization control in current-generation ICF-class laser system configurations; (ii) methods, and their limitations, of TSRS suppression and (iii) optimal geometries to guide future designs.

Keywords: transverse stimulated Raman scattering; large-aperture laser systems; laser damage; KDP; DKDP

1. Introduction

In large-aperture, high-energy laser systems, such as those used in inertial confinement fusion (ICF)-class laser systems, potassium dihydrogen phosphate (KDP) and its deuterated analog (DKDP) are commonly used owing to their ability to grow in large-size crystal boules and because of their high nonlinear coefficients[1]. As a result, KDP and DKDP crystal plates are utilized for second- and third-harmonic frequency generation (THG) and polarization control. As high-fluence laser light propagates through large-aperture (greater than 300 mm) crystal plates, spontaneously scattered light from the dominant A_1 Raman mode, associated with the totally symmetric 'breathing mode' of the PO_4 group, can experience high gain across the transverse dimensions of the plates. This stimulated Raman scattering process involves all photon paths, or propagation angles, confined within the plates via internal reflections from their surfaces, which, in the presence of the large-aperture laser beam propagating

throughout the optic, introduces long amplification paths and, thus, high gain[2]. For a specific plate size and shape, the gain of this transverse stimulated Raman scattering (TSRS) is a function of the crystal cut orientation, which governs the 3D distribution of the spontaneous Raman cross-section and the laser parameters, including the wavelength and polarization state. As the spontaneous Raman cross-section rapidly increases with decreasing laser wavelength, TSRS in ICF-class systems becomes of concern in the ultraviolet section of the laser system, starting with the crystal plate converting the laser energy to the third harmonic[3]. Due to the splitting of the A_1 mode with the introduction of deuterium in the crystal, the peak Raman cross-section is lower in DKDP compared to that in KDP. As a result, DKDP is used for THG in the more powerful laser systems, such as the National Ignition Facility (NIF) and Laser Mégajoule (LMJ)[4,5]. Furthermore, limited experiments exploring the use of DKDP for polarization control at the third harmonic showed prohibitively high TSRS gain and damaged optics and surrounding holders. On the other hand, KDP is successfully employed for harmonic generation and polarization control in lower-output-power laser systems, such as the OMEGA Laser System[6].

Correspondence to: Hu Huang, Laboratory for Laser Energetics, University of Rochester, 250 East River Road, Rochester, NY 14623–1299, USA. Email: huhu@lle.rochester.edu

TSRS amplification is a coherent process that grows exponentially and is distributed nonuniformly in the crystal and at the crystal surfaces. Due to this exponential growth, the fluence level of the TSRS signal reaching the crystal perimeter can vary from harmless levels to ones that cause damage to the crystal or ablation of mechanical components in the vicinity. Methods to manage the TSRS effect have been developed for the THG plate by beveling the edges of the crystal to avoid back-reflections, and thus additional amplification, during the laser pulse[3]. More recently, innovative ideas for TSRS management have emerged and include the introduction of a laser-induced damage array composed of numerous pinpoints inside the plate to form a barrier to prevent signal amplification[7]. A second approach introduces a polarization element at the fundamental frequency, which divides each beam into several sub-beams whose polarization directions are orthogonal as they propagate through the two subsequent frequency triplers[8]. However, these proposed solutions can introduce significant unintended consequences, such as beam-intensity modulations.

Detailed studies to understand such TSRS and its distribution for a specific crystal application configuration have been very limited[9]. To understand the performance limits of current-generation systems and in anticipation of the next-generation ICF lasers for basic research and possible inertial fusion energy production, the understanding and the management of the growth and spatial distribution of TSRS energy are of fundamental importance. In this work, a modeling approach is discussed and used to simulate TSRS generation for several practical configurations, such as harmonic generation and polarization control. The results of this study provide information on the angular dependence of TSRS as a function of the crystal cut orientation and pump polarization. Based on these results, we explore approaches to minimize the TSRS gain and growth in current-generation designs and configurations.

2. Raman generation and amplification in birefringent crystals: the 3D cross-section functions

Stimulated Raman scattering is a process that involves amplification of the spontaneous Raman signal of a particular vibration mode, typically the mode that produces the highest intensity. The spatial distribution of the spontaneous Raman energy is a function of the incident and emitted electric-field polarizations and the directions of incident and emitted waves and quantified by the scattering cross-section, σ_{mol}, of one crystal molecule in the following form:

$$\sigma_{mol} = A_{mol} \cdot |E_P \cdot R \cdot E_R|^2, \tag{1}$$

where A_{mol} is the peak value of the cross-section per molecule, R is the normalized 3×3 Raman polarizability tensor and E_P and E_R are the unit electric polarization vectors

of the pump and scattered light, respectively. Alternatively, the peak value of the cross-section by volume, $A_{vol} = A_{mol}M$, is also used, where M is the molecular density.

Raman scattering in KDP and DKDP has been extensively studied, but the Raman scattering tensor of the dominant A_1 vibration mode was only recently accurately measured following more than four decades of effort. The complexity of the measurement was due to the birefringence in KDP that causes signal artifacts, as detailed in previous work[10]. Efforts also focused on the measurement of the TSRS gain in KDP and KDP, including a quantitative measurement of the peak value of the Raman cross-section at different wavelengths[11,12]. The normalized Raman tensor for this mode in the crystal frame is as follows:

$$R(A_1) = \begin{pmatrix} 1 & 0 & 0 \\ 0 & 1 & 0 \\ 0 & 0 & B \end{pmatrix}, \tag{2}$$

where B is 0.79 (0.76) for KDP (DKDP)[8].

KDP and DKDP are birefringent materials in which the polarizations of orthogonal modes are along the ordinary (o) and extraordinary (e) directions. The o-polarization electric-field vector is normal to both the k vector and the crystal optic axis, and the e-polarization electric-field vector is normal to both the k vector and the o-polarization vector (Figure 1). The index of refraction for the e-polarization depends on the direction of propagation, so the o- and e-components travel at different velocities. During the pump laser pulse, Raman photons are generated into these two polarization modes and amplified by separate gain coefficients (to be discussed later). Because of the velocity difference, the two pump polarization components quickly lose their phase relationship as they travel from the point at which the pump ray enters the crystal to the point in the crystal that generates the spontaneous Raman scattering. Thus, the Raman scattering is effectively separated into the
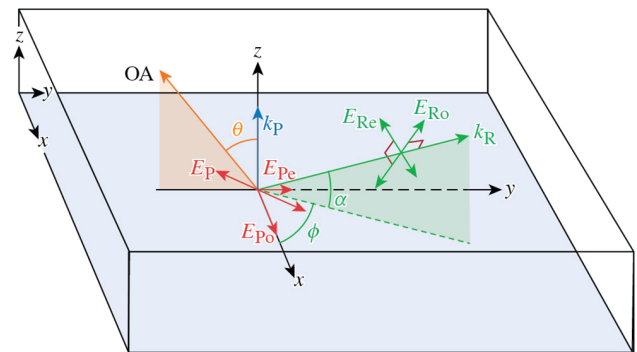
G13830J1

Figure 1. Crystal and laser pump configurations showing the decomposition of the pump and Raman scattering into respective ordinary (o) and extraordinary (e) components. The optic axis (OA) is in the x–z plane, and the Raman k vector k_R can be in any direction.

two incoherent (o and e) components as determined by the pump beam orientation (see Section 6).

The pump o- and e-polarization unit vectors are defined as the following vector products:

$$\boldsymbol{o}_P = \boldsymbol{k}_P \times \overrightarrow{OA}, \quad \boldsymbol{e}_P = \boldsymbol{k}_P \times \boldsymbol{o}_P, \quad (3)$$

where $\boldsymbol{k}_P$ and $\overrightarrow{OA}$ are the unit vectors for the pump $\boldsymbol{k}$ vector and the crystal optic axis, respectively.

In a similar manner, the Raman scattering (or TSRS) generated and propagating in a specific direction is also broken into o- and e-components. As with the pump light, the Raman o- and e-components generated have no fixed phase relationship as they propagate from the source point to the point at which they exit the crystal:

$$\boldsymbol{o}_R = \boldsymbol{k}_R \times \overrightarrow{OA}, \quad \boldsymbol{e}_R = \boldsymbol{k}_R \times \boldsymbol{o}_R. \quad (4)$$

The generated o- and e-components of the spontaneous Raman (or TSRS) signal at any point receive contributions from both the o- and e-components of the pump excitation. These values are determined by the Raman cross-section in the direction of the ray for each Raman and pump polarization. However, as discussed above, both the pump polarization and Raman polarization undergo polarization evolution due to the birefringence of the material. As a result, the o- and e-components of the integrated (total) Raman cross-section generated within a unit volume can be expressed as two separate functions.

For the o-Raman polarization:

$$\sigma_o(\boldsymbol{k}_R) = A_{vol} \cdot \left[|(\boldsymbol{E}_P \cdot \boldsymbol{o}_P) \cdot (\boldsymbol{o}_P \cdot \boldsymbol{R} \cdot \boldsymbol{o}_R)|^2 \right.$$
$$\left. + |(\boldsymbol{E}_P \cdot \boldsymbol{e}_P) \cdot (\boldsymbol{e}_P \cdot \boldsymbol{R} \cdot \boldsymbol{o}_R)|^2 \right] = A_{vol} \cdot Q_o(\boldsymbol{k}_R). \quad (5)$$

For the e-Raman polarization:

$$\sigma_e(\boldsymbol{k}_R) = A_{vol} \cdot \left[|(\boldsymbol{E}_P \cdot \boldsymbol{o}_P) \cdot (\boldsymbol{o}_P \cdot \boldsymbol{R} \cdot \boldsymbol{e}_R)|^2 \right.$$
$$\left. + |(\boldsymbol{E}_P \cdot \boldsymbol{e}_P) \cdot (\boldsymbol{e}_P \cdot \boldsymbol{R} \cdot \boldsymbol{e}_R)|^2 \right] = A_{vol} \cdot Q_e(\boldsymbol{k}_R). \quad (6)$$

where A_{vol} is the volumic Raman scattering coefficient in KDP at 355 nm[10,12]. Equations (5) and (6) provide the general formulation for the Raman cross-section function in any 3D configuration between the pump and Raman propagation directions and the crystal optic axis.

To verify these formulae, cross-section values for the in-plane directions were experimentally measured with spherical crystal samples[13]. This measurement was carried out in the x–z plane (which means the Raman $\boldsymbol{k}$ vector is in this plane). Separate measurements were made to quantify the vertical (z) and the horizontal (in-plane) polarization components. Agreement between experiments and theory provides the basis for quantitative evaluation of the Raman scattering cross-section and TSRS gain in three dimensions.
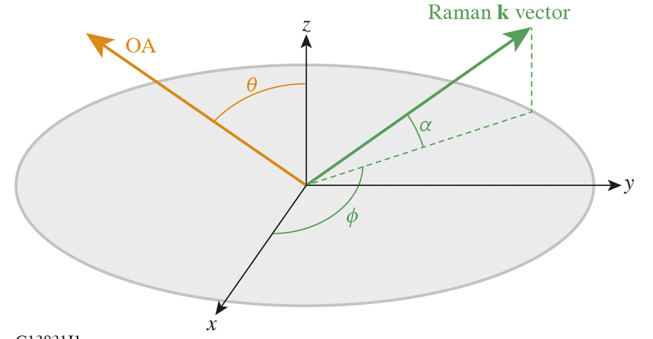

G13831J1

Figure 2. The Raman cross-section function for a specific crystal cut orientation (quantified by the OA angle θ) is defined for any direction in the 3D space for each Raman polarization using two coordinates, the azimuthal angle, ϕ, and the internal angle, α.

The azimuthal angle (ϕ) and the internal angle (α) are used to define a Raman propagation direction over 4π solid angles, as depicted in Figure 2. In the latter part of this paper, we are only concerned with rays that undergo total internal reflections (TIRs) inside the plate (thus for $\alpha < 42°$) because rays outside this range will lose energy after experiencing multiple reflections between the top and bottom surfaces of the crystal plate. Ray paths that do not support TIR are not considered as contributors to TSRS.

Figures 3 and 4 show the 3D normalized cross-section functions for the full 4π solid angle. The strong dependence for both polarizations provides the basis for the later discussion of optimization by choosing the OA tilt angle to reduce TSRS.

3. Raman gain factor

Let us consider a Raman ray that has been generated in a volume element dV during a time interval dt. This ray travels in the direction of $\boldsymbol{k}_R$ as a cone for a distance l inside the crystal, and has a solid angle element of dΩ. The initial spontaneous Raman emission (d$E^o_{TSRS\,o,e}$) has two components, o and e, that are related to the normalized cross-sections for o and e as discussed in the previous section:

$$dE^o_{TSRS\,o,e}(\boldsymbol{k}_R) = A_{vol} \cdot Q_{o,e}(\boldsymbol{k}_R) \cdot dt \cdot I_{pump} \cdot dV \cdot d\Omega, \quad (7)$$

where $Q_{o,e}$ are the normalized cross-section functions for the o- and e-Raman polarization components (Equations (5) and (6)) expressed in the previous section and I_{pump} is the pump intensity. The d$E^o_{TSRS\,o,e}$ contains the dependence of the Raman signal on the relative directions of the vectors involved ($\boldsymbol{k}$ vector, $\overrightarrow{OA}$ and polarization vectors).

After this ray propagates by a length l, its Raman radiation energies (d$E^o_{TSRS\,o,e}$) are the corresponding initial emitted energies (Equation (7)) multiplied by the exponential gain factor for each individual polarization, which is
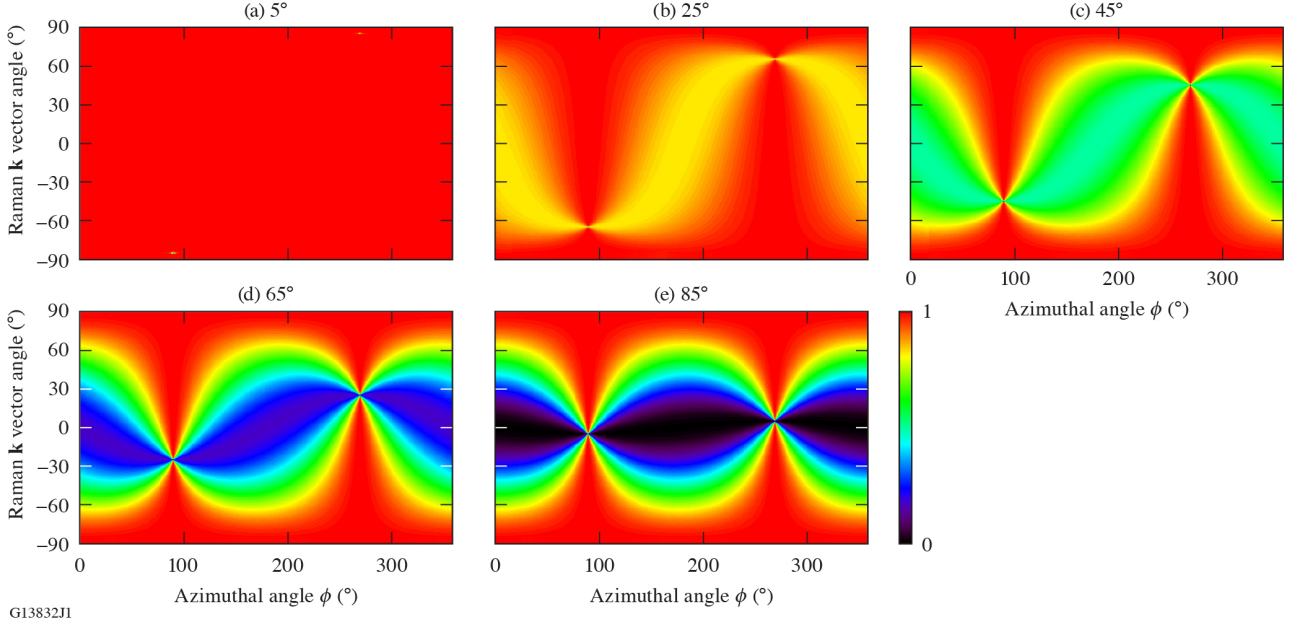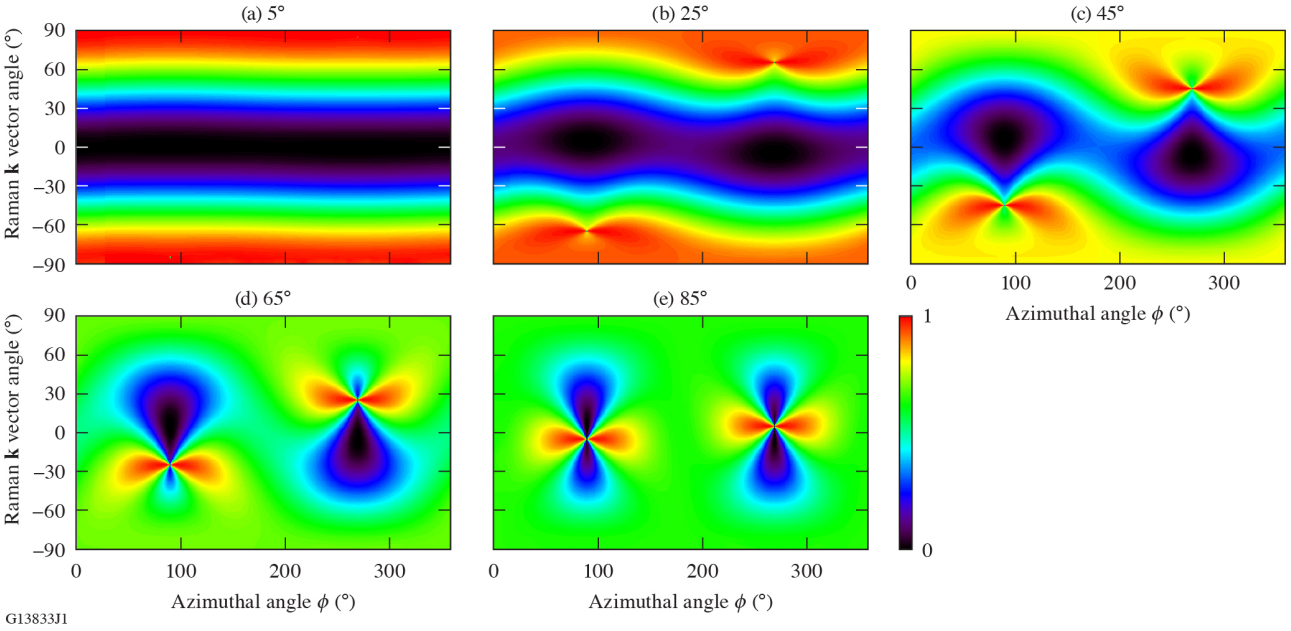
Figure 3. The normalized Raman scattering cross-section function (maximum value is 1) in three dimensions calculated for the o-polarization component as a function of the optic axis (θ) orientation.

Figure 4. The normalized Raman scattering cross-section function (maximum value is 1) in three dimensions calculated for the e-polarization component as a function of the optic axis (θ) orientation.

governed by the propagation length, the laser intensity I_{pump} and the Raman gain coefficient:

$$dE^l_{TSRS\,o,e}(\boldsymbol{k}_R) = dE^o_{TSRS\,o,e}(\boldsymbol{k}_R)$$
$$\cdot \exp\left[\frac{8\pi cM}{h\omega_R^3 n_{o,e}^2 \Delta\nu} I_{pump} A_{mol} Q_{o,e}(\boldsymbol{k}_R)\, l\right]$$
$$= dE^o_{TSRS\,o,e}(\boldsymbol{k}_R) \cdot \exp\left[I_{pump} g Q_{o,e}(\boldsymbol{k}_R)\, l\right]. \tag{8}$$

Here, g is the generally accepted notation for the gain coefficient with the dimension of cm/GW:

$$g = \frac{8\pi cM}{h\omega_R^3 n_{o,e}^2 \Delta\nu} A_{mol}, \tag{9}$$

where c is the speed of light, M is the molecular density, h is the Planck constant, ω_R is the Raman angular velocity, $n_{o,e}$ is the crystal index of refraction and $\Delta\nu$ is the bandwidth of the
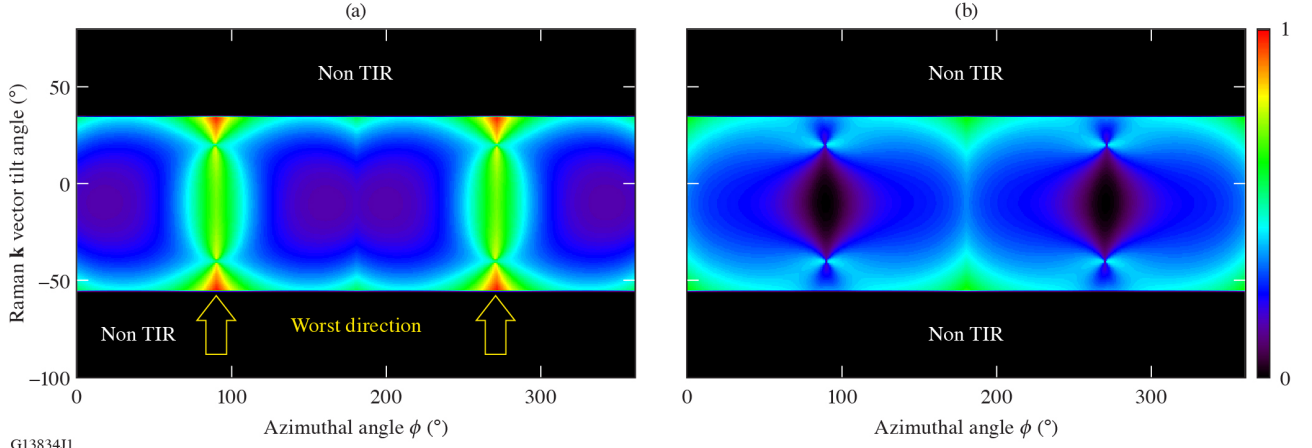
Figure 5. Example case of the estimation of the gain factors assuming a source point at the middle of the plate for the (a) o-polarization and (b) e-polarization components as a function of the azimuthal angle (ϕ) and the ray tilt angle (α) for a square crystal plate with the OA angle (θ) at 60° and pump polarization in the 45° diagonal direction.

A_1 mode expressed as wave numbers. The gain coefficient g has the dimension of cm/GW.

We now combine the contributions of the normalized cross-section functions and the propagation length to define $G_{o,e} = Q_{o,e}l$ as the gain factor. This factor contains all the dependence of vectors in Figure 1 and includes the contribution of the path length.

In a ray-tracing calculation, we consider N rays generated in a crystal unit volume dV and during a time interval dτ that is a fraction of the pump pulse duration τ. The generated rays are propagating in a 4π solid angle with the initial Raman energy (generated within ΔV and $\Delta \tau$) in the o- or e-polarization, expressed as follows:

$$E_{\text{TSRS o,e}}^{\text{o}}(\boldsymbol{k}_{\text{R}}) = 4\pi \, \Delta V \cdot \Delta \tau \cdot I_{\text{pump}} \cdot A_{\text{vol}} \cdot Q_{\text{o,e}}. \quad (10)$$

For conservation of energy, we assume that the energy of each ray propagating along a direction $\boldsymbol{k}_{\text{R}}$ is $E_{\text{TSRS o,e}}^{\text{o}}(\boldsymbol{k}_{\text{R}})/N$. The total Raman energy generated by a pulse of length τ is the sum (integral) over all volume elements, solid angles and initial time when the Raman seed signal is generated for both o- and e-ray spontaneous Raman energy (Equation (7)) multiplied by the gain factor $\exp(I_{\text{pump}} \cdot g \cdot G_{\text{o,e}})$. This sum should converge to be independent of N when the sample ray density is sufficiently large. In the numerical calculations in Section 5 over 30,000 rays were used for each data point and doubling the number of rays changed the results by less than 1%.

As an illustration to help understand the distribution of generated Raman scattering at the edge of the crystal, let us consider a source point in the middle of a square plate. The normalized gain factor is calculated for all TIR directions (both α and ϕ) from this source point to the edges of the plate. Figure 5 shows this normalized gain factor for the case of a square plate with the OA on the y–z plane with tilt angle of 60° and pump polarization along the diagonal direction of the plate ($\phi = 45°$). The location of the maximum value of

G_{o} is at $\phi = 90°$ and $\phi = 270°$ (indicated with arrows), while G_{e} presents a much lower value. We notice that the range of angles with a significant gain factor is restricted to a rather narrow area (solid angle) near the limit of the TIR condition. This pattern depends on the location of the source point. For each different configuration (i.e., crystal geometry, OA cut and pump laser polarization), the distribution patterns of the gain factors can be determined and used to calculate the accumulated TSRS energy around the edges of the crystal.

Additional considerations for modeling the gain factor assuming square optics are as follows:

(i) the path length of a specific ray from one side to the other side is $D/\cos(\alpha)\cos(\phi)$ (Figure 5);

(ii) the gain of rays confined by TIRs is the averaged values between the two principal directions (toward and away from the input surface of the plate);

(iii) combining these two effects, the maximum path length of all rays is approximately $2D$.
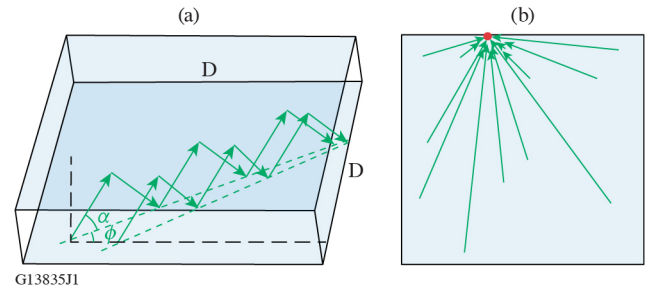
This is shown in Figures 6(a) and 6(b).

Figure 6. Considerations for modeling the gain factor assuming square optics where (a) shows the different photon propagation paths involving total internal reflections and (b) the signal arriving at any point in the side surfaces of the plate is considered a superposition of all rays arriving at this point that were generated in different parts of the crystal volume.

4. Ray-tracing modeling details

The ray-tracing model utilizes a volume grid (element) for the bulk of the crystal and a surface grid for the side surfaces of the crystal. The amount of Raman signal (energy) originated from each ray (starting from a volume element during a time interval to eventually arrive at the surface element) is proportional to the pump intensity, the volume element size, the time interval, the cross-section for this ray direction and the solid angle element associated with the surface element extending from the source point. For a ray that is confined via TIR between the top and bottom surfaces, this solid angle is the surface element area projected to the normal direction of the ray, divided by the total path length. Rays from different locations in the crystal plate arrive at the same sampling point at a side surface. This process is depicted in Figure 6(b) where each arrow represents many rays that have different TIR internal angles, as shown in Figure 6(a).

For each source point and a given internal angle, a pair of rays (o and e) is generated at one time interval during the pump pulse. Each is amplified by its corresponding gain until they arrive at the next TIR point on the top or bottom surface. At this point the o- and e-rays are projected to the s and p polarization directions (related to the beam incidence on the surface). Following a TIR, the reflected rays become s' and p', where s' remains the same as s but p' changes direction from p by 2α. From s' and p' we reconstitute o' and e' intensities and continue the ray propagation using the gains for the new direction. The total TSRS reaching a sampling area element is the sum of all rays reaching this location from all source points and angles and includes consideration of the time at which the initial spontaneous Raman photon is generated during the pulse length. Rays initiated during the pulse are amplified for the part of pulse between its starting moment until the end of the pulse or until it hits the sampling area, whichever is earlier.

Within this modeling, side surfaces are considered but reflections at the edge surfaces are not. When a ray reaches the sampling point on the edge, we add both o- and e-intensities. We assume a 40 cm × 40 cm × 1 cm plate and use a 3-ns pump pulse, as used by Dixit *et al.*[9]. This interval is the time required for light to travel across the plate parallel to the surface. There are, however, rays that take longer than 3 ns to reach an edge. For example, a ray that zigzags from one corner to the opposite corner takes approximately 4 ns to propagate. When the 3-ns pump pulse is over, those rays that have not reached any of the four edge surfaces continue until they reach one of those edges, but there is no further amplification. As we showed in the previous section, the rays with a maximum internal angle, and consequently a longer path length, contribute to TSRS most significantly. We first use this model to simulate the most detailed results available to date on TSRS presented by Dixit *et al.*[9]. Although the exact locations of the measurements are not included in this

manuscript, we use the gains and cross-sections that would fit their data, as follows.

KDP: cross-section $A_{vol} = 3.47 \times 10^{-7}$ cm^{-1} sr^{-1}, gain $g = 0.347$ cm/GW

DKDP (70%): cross-section $A_{vol} = 2.9 \times 10^{-7}$ cm^{-1} sr^{-1}, gain $g = 0.203$ cm/GW

These values are then used in our modeling to generate detailed data for various situations.

5. Results of modeling

Let us first consider the third-harmonic crystal configuration used on the NIF laser, which has the 3ω polarization oriented in the y direction (see Figure 2). The incident 1ω and 2ω rays at the front surface are converted into 3ω as they propagate through the plate[14] and the 3ω light only reaches its full power at the exiting surface of the crystal plate. We incorporate this 3ω distribution in our modeling to calculate the TSRS distribution in the side surfaces of the crystal. In the plots shown in Figure 7, the TSRS values are given in arbitrary units since the focus of this study is to determine the comparative TSRS values between the existing THG and proposed polarization rotating devices. Also, because the details of the NIF measurements presented in Ref. [9], such as how and where the measurement was obtained (there is a great variation of intensity distribution at the edges, as shown by the results), are not available and the model results are based on certain assumptions discussed earlier, we think it is more prudent not to use absolute values.

Figure 7 shows the TSRS distributions for the THG configuration for different pump intensity levels. The inset shows a schematic depiction of the crystal configuration, where the pump polarization is along the y-axis and the OA orientation is at an angle of $\theta = 59°$ along the z–y plane. The results show that the TSRS intensity varies within the crystal side surfaces and reaches maximum intensity in the middle regions of the x side along the y-axis. It is thus expected that significant TSRS gain will be first generated along this direction.

Next, we consider the TSRS for a wave-plate configuration suitable for 90° rotation of polarization at 3ω. In this configuration (Figure 8), the crystal OA is in the plane that cuts through the diagonal line of the plate. With the OA at $\theta = 10°$ (Figure 8(a)), two corners receive several orders of magnitude higher TSRS compared to that observed for the THG configuration. With the OA at $\theta = 90°$ (Figure 8(b)), the variation of TSRS along each side is not significant, but the average value is even higher. It is appreciated that the spatial distribution along the edge surfaces parallel to both the x-axis and the y-axis is symmetric and that the maximum intensity is observed along the diagonal direction.

Since the TSRS distribution depends on the direction of the OA, we explored the change of its peak value as a function of the OA tilt angle, as shown in Figure 9. These
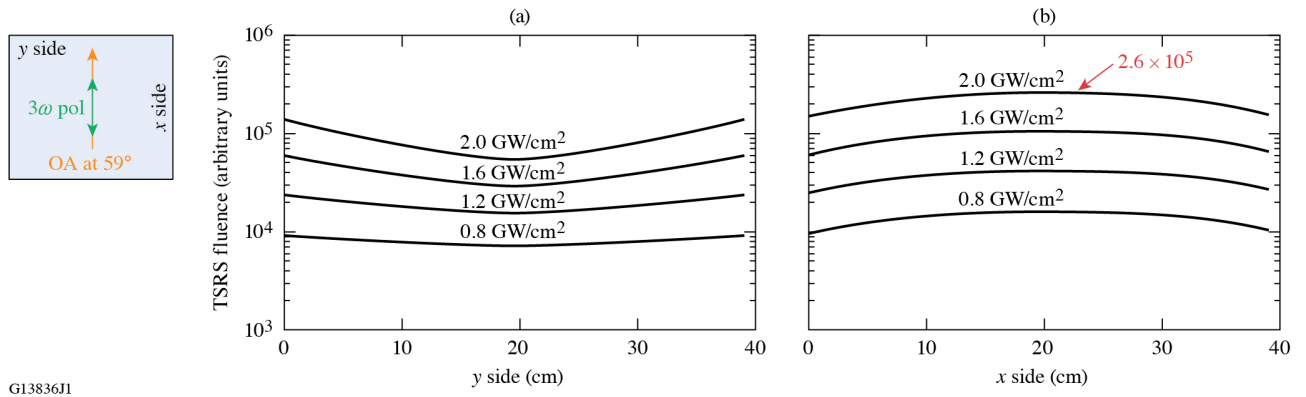
Figure 7. TSRS fluence distribution along the (a) *x*-axis and (b) *y*-axis surfaces for THG crystal configuration (depicted in the inset, beam propagating into the page) under various pump pulse energy levels.
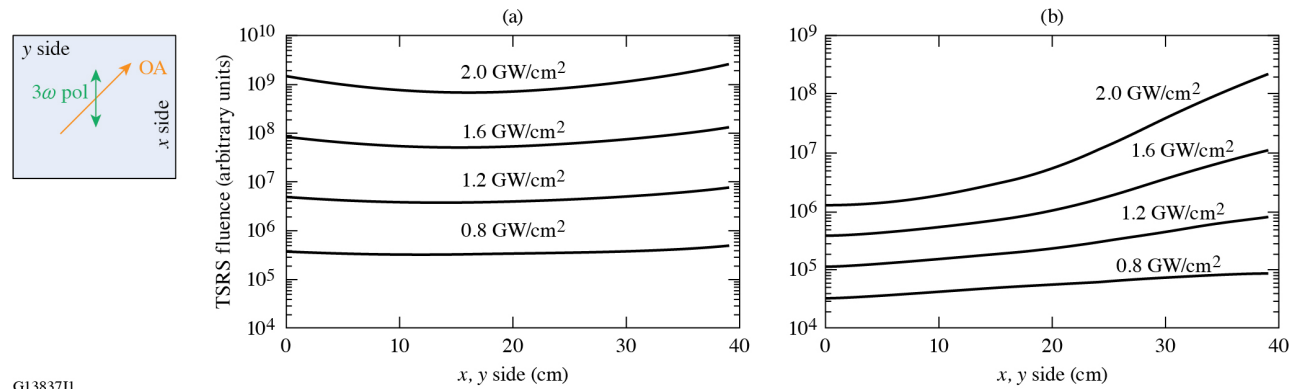
Figure 8. TSRS fluence distribution along the crystal side surfaces for wave-plate crystal configuration (depicted in the inset, beam propagating into the page) under various pump pulse energy levels with the optic axis tilted by (a) 10° and (b) 90°. The maximum fluence is along the diagonal direction orthogonal to the direction of the OA.
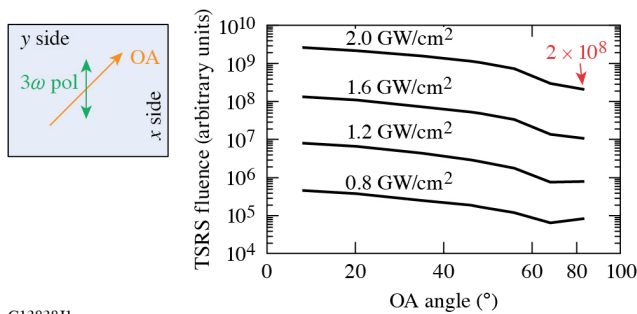
Figure 9. The maximum TSRS fluence as a function of the OA tilt angle for the case of a wave-plate crystal configuration (depicted in the inset, beam propagating into the page) for DKDP.

results show that by using a $\theta = 90°$ (OA tilt angle), the TSRS can be reduced by more than a factor of 10. However, the TSRS level is still several orders of magnitude higher than the tripler configuration (see Figure 7(b)).
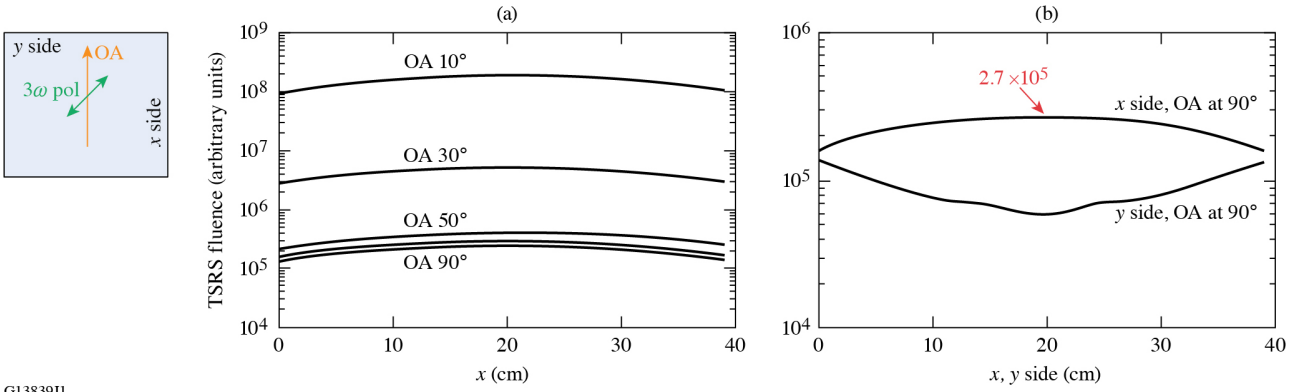
An alternative configuration for the wave plate can be considered by assuming the beam polarization is at 45° and the OA is in the *y–z* plane, as depicted by the inset of Figure 10, where the OA tilt angle is used as a parameter for optimization. As can be seen from the results shown in

Figure 10, this configuration makes it possible to have a wave plate that produces maximum TSRS at 2 GW/cm², similar to that of the tripler.

These results can be viewed in two different ways. Firstly, we can examine the maximum TSRS fluence for a fixed pump level (of 2 GW/cm²) and consider that of the tripler crystal as the reference value, since the tripler is inevitably going to be part of the laser system (see Table 1). We can also examine the maximum possible pump level for each configuration that will facilitate the same maximum TSRS, which in this case is considered to be that of the tripler for a pump intensity of 2 GW/cm². Arguably, these results provide a better understanding on the TSRS-induced limitations of current systems and guide potential paths forward.

6. Discussion

The TSRS can be treated as an incoherent superposition of the two polarization components, both temporally and spatially. In reality, Raman emission and amplification have finite spatial and temporal coherences, which have been discussed extensively by Raymer *et al.*[15]. The degree of

Figure 10. TSRS fluence distribution (a) along the x side surface for an alternate DKDP wave-plate configuration (depicted in the inset, beam propagating into page) for various OA tilt angles assuming an intensity of 2 GW/cm^2 and (b) along the x and y sides for the case of OA tilt angle of 90°.

Table 1. The TSRS fluence for a DKDP plate, 40 cm × 40 cm × 1 cm, for the THG configuration, the conventional wave-plate configuration and the optimized wave-plate configuration considering a fixed pump intensity (2 GW/cm^2) or a fixed maximum TSRS fluence ($\approx 2.5 \times 10^5$).

DKDP (40 cm × 40 cm × 1 cm)	TSRS fluence (arbitrary units)	I (GW/cm^2)
Tripler/NIF-like geometry	2.6×10^5	2
Wave-plate/NIF-like geometry	2×10^8	2
Wave-plate/NIF-like geometry	2.5×10^5	1
Wave-plate/optimized geometry	2.7×10^5	2

spatial coherence and intensity modulation depend on the geometry of the medium where the Raman scattering is generated and amplified. A square meter-scale crystalline plate, used in large aperture solid-state laser systems, generally has a low degree of Raman spatial coherence at the plate's edge. On the other hand, a long cylindrical medium, such as laser propagation over long air paths, tends to have a higher degree of Raman spatial coherence at its end. Based on Raymer's theory, we conclude that the TSRS in the ICF plates has weak coherent effects, both spatially and temporally. The time-integrated speckle intensity contrast is calculated to be in the range of a few percent or lower. Thus, this additional factor does not significantly affect our conclusions.

The aim of this work is to demonstrate a method to quantitatively evaluate TSRS in a configuration relevant to large-aperture laser systems. The specific case examples presented herein were focused on simulating the most detailed results available to date on TSRS generation in large-aperture laser systems presented by Dixit *et al.*[9]. For this reason, we assumed a 40 cm × 40 cm × 1 cm plate and used a 3-ns flat in time pump pulse with a uniform spatial beam profile. We are also seeking the TSRS conditions at the onset of strong nonlinear amplification. Thus, we do not consider the depletion of the pump or filamentation of the pump. The model can be readily modified to include temporal and

spatial variations of the pump. However, depletion of the pump is a more difficult problem because it breaks the independent evolution of Raman rays and makes parallel computation invalid.

In this work we are also not considering amplification of the reflected TSRS back to the crystal at the edges. This can be a major technical challenge and can be mitigated using various methods that have already been utilized, such as edge cladding, beveling, antireflection coatings or special cuts of the crystal to direct reflection of the 'worst rays' in directions that do not support additional gain. Another solution to be explored is to apply an index-matched absorptive coating on plate edges to further reduce TSRS propagation. Such index-adjustable absorptive paint has been developed and is available[16,17]. Furthermore, controlling the pulse shape can be an additional tool. Ultimately, there are a number of ways to design wave plates that suppress TSRS gain that may also require control of the incoming polarization state with respect to the geometric orientation of the plate (such as the rotation of pump polarization by 45° discussed above). The general method presented in this work can be applied in a variety of designs and specific excitation parameters.

Finally, it must be noted that the laser-induced damage on the material is based on the total local fluence with contributions from all wavelengths. Given the small shift in energy between the pump beam and the generated TSRS (associated with a shift in wavelength of about 12 nm), the damage probability should be considered as the sum of TSRS and pump fluences. In addition, unconverted second-harmonic light will also contribute, to a lesser extent, to the damage initiation process[18]. Once damage is initiated and plasma is formed, the remaining unconverted fundamental and second-harmonic beams will strongly contribute to the energy deposition process due to absorption by the formed plasma, and thus the final size of the damage site. One should also consider that the laser-ablation threshold of metals that may be used in optic mounts is very low (of the order of

250 mJ/cm^2). As a result, even a small amount of TSRS, which does not pose a direct concern for the optic that escapes from the side surfaces of the plate, can initiate contamination of the optic by particles generated from the ablation of metal holders. These particles can subsequently initiate damage (and downstream beam modulation) that can also have a detrimental effect on the lifetime of the optic and the laser system in general. Thus, it is imperative that the spatial distribution of the TSRS for a particular system geometry is considered in the design of the mounts and the selection of materials used for mounting.

7. Conclusion

TSRS in laser crystal optics grows exponentially with the pump fluence and can cause damage to laser components. An incoherent propagation model for TSRS that allows the determination of the Raman cross-section and gain in any direction in three dimensions is constructed. Ray-tracing calculations utilizing these cross-sections and gain values lead to the determination of TSRS generated in a crystal during a pulse as well as the distribution of TSRS fluence at the edges of the crystal plate.

By varying crystal configuration parameters, we can minimize the TSRS in distributed polarization ratios to be used in current high-power laser systems.

Acknowledgements

References

1. L. J. Atherton, A. K. Burnham, R. C. Combs, S. A. Couture, J. J. De Yoreo, R. A. Hawley-Fedder, R. C. Montesant, H. F. Robey, M. Runkel, M. Staggs, P. J. Wegner, M. Yan, and N. P. Zaitseva, "Producing KDP and DKDP crystals for the NIF laser," Report UCRL-ID-135590 (Livermore National Laboratory, Livermore, CA, 1999).
2. C. E. Barker, R. A. Sacks, B. M. Van Wonterghem, J. A. Caird, J. R. Murray, J. H. Campbell, K. R. Kyle, R. B. Ehrlich, and N. D. Nielsen, Proc. SPIE **2633**, 501 (1995).
3. S. Tang, Y. Guo, X. Jiang, L. Yang, and B. Zhu, in *Conference on Lasers and Electro-Optics* (Optica Publishing Group, 2018), paper JTu2A.178.
4. M. L. Spaeth, K. R. Manes, D. H. Kalantar, P. E. Miller, J. E. Heebner, E. S. Bliss, D. R. Speck, T. G. Parham, P. K. Whitman, P. J. Wegner, P. A. Baisden, J. A. Menapace, M. W. Bowers, S. J. Cohen, T. I. Suratwala, J. M. Di Nicola, M. A. Newton, J. J. Adams, J. B. Trenholme, R. G. Finucane, R. E. Bonanno, D. C. Rardin, P. A. Arnold, S. N. Dixit, G. V. Erbert, A. C. Erlandson, J. E. Fair, E. Feigenbaum, W. H. Gourdin, R. A. Hawley, J. Honig, R. K. House, K. S. Jancaitis, K. N. LaFortune, D. W. Larson, B. J. Le Galloudec, J. D. Lindl, B. J. MacGowan, C. D. Marshall, K. P. McCandless, R. W. McCracken, R. C. Montesanti, E. I. Moses, M. C. Nostrand, J. A. Pryatel, V. S. Roberts, S. B. Rodriguez, A. W. Rowe, R. A. Sacks, J. T. Salmon, M. J. Shaw, S. Sommer, C. J. Stolz, G. L. Tietbohl, C. C. Widmayer, and R. Zacharias, Fusion Sci. Technol. **69**, 25 (2016).
5. J. L. Miquel, C. Lion, and P. Vivini, J. Phys.: Conf. Ser. **688**, 012067 (2016).
6. M. J. Guardalben, M. Barczys, B. E. Kruschwitz, M. Spilatro, L. J. Waxer, and E. M. Hill, High Power Laser Sci. Eng. **8**, e8 (2020).
7. W. Han, L. D. Zhou, F. Q. Li, J. Wang, F. Wang, and B. Feng, Laser Phys. **23**, 116001 (2013).
8. X. Fan, S. Li, X. Huang, J. Zhang, C. Wang, H. Li, Y. Sun, and H. Sun, Laser Part. Beams **36**, 454 (2018).
9. S. N. Dixit, D. Munro, J. R. Murray, M. Nostrand, P. J. Wegner, D. Froula, C. A. Haynam, and B. J. MacGowan, J. Phys. IV France **133**, 717 (2005).
10. T. Z. Kosc, H. Huang, T. J. Kessler, R. A. Negres, and S. G. Demos, Sci. Rep. **10**, 16283 (2020).
11. S. G. Demos, R. N. Raman, S. T. Yang, R. A. Negres, K. I. Schaffers, and M. A. Henesian, Proc. SPIE **8190**, 81900S (2011).
12. S. G. Demos, R. N. Raman, S. T. Yang, R. A. Negres, K. I. Schaffers, and M. A. Henesian, Opt. Express **19**, 21050 (2011).
13. T. Z. Kosc, H. Huang, T. J. Kessler, and S. G. Demos, Opt. Express **30**, 12918 (2022).
14. R. S. Craxton, IEEE J. Quantum Electron. **17**, 1771 (1981).
15. M. G. Raymer, I. A. Walmsley, J. Mostowski, and B. Sobolewska, Phys. Rev. A **32**, 332 (1985).
16. K. Ramadurai, C. L. Cromer, L. A. Lewis, K. E. Hurst, A. C. Dillon, R. L. Mahajan, and J. H. Lehman, J. Appl. Phys. **103**, 013103 (2008).
17. J. L. Lyon, P. A. Maurey, W. Senaratne, A. L. Weikel, and Y. Zhang, U.S. Patent No. 10,377,913 B2 (13 August 2019).
18. P. DeMange, R. A. Negres, A. M. Rubenchik, H. B. Radousky, M. D. Feit, and S. G. Demos, J. Appl. Phys. **103**, 083122 (2008).